International Core Journal of Engineering Volume 11 Issue 6, 2025
ISSN: 2414-1895 DOI: 10.6919/ICJE.202506_11(6).0022

Study on Process Parameter Optimization in Laser Additive Manufacturing of 7075 Aluminum Alloy

Shaoting Cao, Weihao Cheng, Lan Zhang

AVIC Chengdu Aircraft Industrial (Group) Co., Ltd., Chengdu 610092, China

Abstract

7075 aluminum alloy has become one of the commonly used lightweight alloys in aerospace applications due to its low density, high specific strength and stiffness, and excellent corrosion resistance. However, owing to its high thermal conductivity, high laser reflectivity, and wide solidification interval, 7075 aluminum alloy is prone to metallurgical defects such as intergranular solidification cracks during laser powder bed fusion (LPBF) processing, which severely affects the forming quality and mechanical properties of the fabricated components. To address these scientific challenges, this study employed LPBF technology to fabricate 7075 aluminum alloy, exploring its optimized processing window and revealing the formation mechanisms of multi-scale metallurgical defects. The effects of varying scanning speeds, laser powers, and laser energy densities on the forming quality and mechanical properties of LPBF-processed 7075 aluminum alloy were systematically investigated. The results indicate that as the laser energy density increases from 119 J/mm³ to 298 J/mm³, the relative density of the samples initially rises and then stabilizes. The optimal relative density of 98.5% is achieved at a laser energy density of 295 J/mm³. Meanwhile, the microhardness of the fabricated specimens significantly increases from 85±3 $HV_{0.1}$ to 104±3 $HV_{0.1}$ with higher energy densities. The optimized process parameters are identified as a laser energy density of 298 J/mm³, a laser power of 425 W, and a scanning speed of 800 mm/s.

Keywords

7075 Aluminum Alloy; Laser Powder Bed Fusion; Microscopic Structure.

1. Introduction

Additive manufacturing (AM) is a production method based on the discrete-stacking principle, where components are fabricated layer by layer through the accumulation of materials[1]. By utilizing a three-dimensional computer model, AM enables the bottom-up, layer-by-layer construction of three-dimensional parts, achieving a form of unconstrained manufacturing[2]. The significant advantages of additive manufacturing include:(1) A substantial reduction in processing steps, eliminating the need for additional molds and tools;(2) A novel "near-net shaping" concept, particularly suitable for fabricating complex structures, customized components, and lightweight metal parts;(3) High material utilization, minimizing waste;(4) From a microstructural perspective, the rapid solidification characteristics of AM result in fine and homogeneous microstructures, endowing fabricated components with superior comprehensive mechanical properties[3]. With the continuous development of additive manufacturing technologies, various methods have emerged. Among these, Laser Powder Bed Fusion (LPBF) stands out as a critical technique in AM. LPBF is a widely adopted laser-based additive manufacturing technology that involves layer-by-layer powder deposition and rapid laser melting, offering immense potential for forming aluminum alloy components. This method exhibits notable advantages in fabricating complex geometries and thin-walled structures[4].

ISSN: 2414-1895 DOI: 10.6919/ICJE.202506_11(6).0022

LPBF primarily targets metallic materials. During LPBF processing, complex physical and chemical interactions occur between the laser and the powder material, forming a melt pool under laser irradiation. The cooling rate within the melt pool can reach 10^3-10^8 K/s[5-6], which suppresses grain growth and segregation while promoting fine and uniform microstructures through Marangoni convection stirring[7]. Compared to Selective Laser Sintering (SLS), LPBF is compatible with a broader range of metal alloys, such as Ti-based alloys[8-9], Ni-based alloys[10-11], and Fe-based alloys[12]. Currently, LPBF has been applied in aerospace, medical, and other fields. In recent years, LPBF processes for aluminum alloys and aluminum matrix composites, such as AlSi10Mg[13-14], have attracted extensive research attention, successfully producing high-density specimens with excellent mechanical properties. However, certain traditional aluminum alloys, such as 7075 aluminum alloy, face challenges due to their inherent characteristics-including high thermal conductivity[15-16], high laser reflectivity[17], and low melt fluidity[18]-resulting in coarse grains, porosity, and cracks during LPBF processing. These defects severely compromise the forming quality and mechanical performance of 7075 aluminum alloy components, making their fabrication particularly challenging.

In LPBF processing of aluminum alloys, parameters such as laser scanning speed, laser power, substrate preheating temperature, and support structures significantly influence thermal crack formation. Identifying the optimal processing window is therefore crucial.

Kaufmann N et al. from the University of Hamburg[16] fabricated EN AW 7075 aluminum alloy specimens via Selective Laser Melting (SLM). Through density measurements and compositional analysis, they explored the optimal SLM parameters for EN AW 7075. The study revealed that lower scanning speeds and higher laser powers improved specimen density. The concept of laser energy density was introduced to evaluate the combined effects of laser power and scanning speed on density. Despite these optimizations, thermal cracks persisted in all longitudinal cross-sections of the specimens. Preheating the substrate from 40 °C to 200 °C showed limited effectiveness in crack suppression.

Wojciech Stopyra et al. from Wrocław University of Science and Technology[19] fabricated single tracks, thin walls, and bulk specimens of 7075 aluminum alloy via LPBF. By analyzing metallography, density, and composition at different processing stages, they identified the optimal LPBF parameters for 7075 aluminum alloy. Single-track experiments were conducted with laser powers of 200 W (scanning speeds: 250 mm/s and 350 mm/s) and 400 W (scanning speed: 250 mm/s). Results showed melt pool depth-to-width ratios of 1.3 (400 W), 0.69 (200 W, 250 mm/s), and 0.3 (200 W, 350 mm/s). The microhardness within the melt pool decreased from 167 HV0.025 to 140 HV0.025 as the depth-to-width ratio decreased. However, microstructural analysis (Fig. 1.6a–c) revealed cracks at the transition zones between fine-grained and columnar regions in melt pools with depth-to-width ratios of 1.3 and 0.69. Keyhole defects were also observed at a depth-to-width ratio of 1.3. Increasing laser power enlarged melt pool dimensions and enhanced hardness but introduced porosity and cracks. Subsequent bulk specimen fabrication (10×10×5 mm) using 200–400 W laser power, 200–600 mm/s scanning speeds, and four scanning strategies (unidirectional, orthogonal, island, and remelting) identified optimal parameters: 200 W, 200 mm/s, 20 μm layer thickness, 140 μm hatch spacing, and island scanning strategy.

Wang Dayuan et al[20] investigated the effects of laser energy density on the forming quality and defects of 7075 aluminum alloy under fixed scanning speed and varying laser power. Results indicated that relative density initially increased and then stabilized with higher laser energy density, reaching a maximum of 97.2% at 137 J/mm³. Segregation-induced non-equilibrium secondary phases (T-phase and η'-phase ($MgZn_2$)) precipitated, contributing to crack formation. Crack length increased with laser energy density, while crack density decreased. Tensile strength improved from 197 MPa to 331 MPa as laser energy density rose from 63 J/mm³ to 137 J/mm³.

This study employs LPBF to fabricate 7075 aluminum alloy specimens with varying scanning strategies, speeds, and laser powers. The effects of laser parameters on densification, surface quality,

ISSN: 2414-1895 DOI: 10.6919/ICJE.202506_11(6).0022

phase composition, and microstructure are systematically investigated. Mechanical properties, including hardness and tensile performance, are analyzed under different processing conditions. Advanced characterization techniques are utilized to examine microstructural evolution and fracture surfaces, ultimately establishing optimized laser processing parameters and metallurgical defect control mechanisms to identify the optimal process thresholds.

2. Experimental Materials and Procedures

2.1 Raw Materials

The quality of powder is a critical factor in determining the forming quality of components fabricated via Laser Powder Bed Fusion (LPBF). Due to the high cost of developing custom powders tailored for LPBF, commercial powders with well-controlled compositions and mechanical properties are commonly used. In this study, 7075 aluminum alloy powder and pure titanium powder, produced by TLS Technik via gas atomization, were employed. The morphology and particle size distribution of the 7075 aluminum alloy powder are shown in Fig. 1. The particle size ranges from 10 μm to 95 μm, with a relatively uniform distribution. The chemical composition of the 7075 alloy is listed in Table 1.

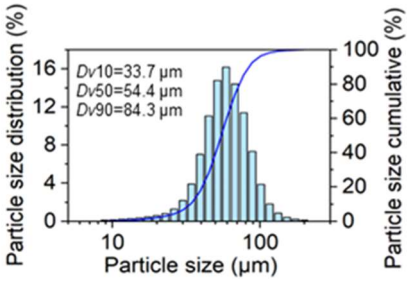

Fig. 1 Particle size distribution of 7075 aluminum alloy powder

Table 1. Chemical composition of 7075 aluminum alloy

Element	Al	Zn	Mg	Cu	Cr
Content(wt.%)	Balance	5.6	2.5	1.6	0.3

2.2 Experimental Design

An initial powder-free scanning strategy (zero powder supply from the feed cylinder) was applied to preheat the substrate. Subsequently, the powder was spread, and after complete melting of the first layer, the build platform descended by one layer thickness. The feed cylinder then ascended to supply powder for the next layer, which was spread using a recoater system. The laser melting process was repeated layer-by-layer until the entire component was formed. To ensure stable powder spreading and laser-powder interaction, the process parameters listed in Table 2 were selected. The volumetric energy density (E, J/mm³), calculated using Equation (1), was employed to evaluate the laser energy input.

$$E = P/vdh. \quad (1)$$

where P is the laser power (W), v is the scanning speed (mm/s), d is the layer thickness (μm), and h is the hatch spacing (μm). To minimize residual stress, a 37° rotated chessboard scanning strategy per layer was adopted. All LPBF processes were conducted under an argon atmosphere to minimize oxygen contamination.

ISSN: 2414-1895 DOI: 10.6919/ICJE.202506_11(6).0022

Table 2. Laser parameters

Laser Power (W)	300/350/400/425
Scanning Speed (mm/s)	800/1000/1200/1400
Layer Thickness (μm)	30
Hatch Spacing (μm)	60
Scanning Strategy	Chessboard, 37° rotation per layer

2.3 Characterization Methods

The relative density of specimens was measured using the Archimedes drainage method. Microstructural analysis was performed using an Olympus Corporation optical microscope. Surface morphology and spheroidization/crack formation under different parameters were examined via Scanning Electron Microscopy (SEM). For phase analysis, the 7075 aluminum alloy specimens were ground, polished, and analyzed using an X-ray Diffraction (XRD) instrument with a copper target (operating at 40 kV and 40 mA). The scanning range was 20–90° 2θ at a rate of 2°/min, followed by detailed scans in the ranges 37–60° 2θ and 60–75° 2θ at 0.5°/min. Data were processed using Jade software and compared with standard PDF cards. Specimens were further polished with argon ions to enhance clarity for subsequent characterization. SEM was also used to analyze melt pool morphology, microstructure, grain structure, and precipitate distribution.

2.4 Mechanical Testing

Microhardness was measured using a Vickers hardness tester under a 0.1 kg load with a 10 s dwell time. For each specimen, multiple indentations were made along a straight line with a spacing of ≥300 μm between points. Lines were spaced 1 mm apart vertically to ensure accuracy. The final hardness value for each specimen was the average of all measurements. Tensile testing was conducted according to ASTM-E8 standards at a crosshead speed of 2 mm/min, with a gauge length of 25 mm. Specimens were polished and tested at room temperature to determine ultimate tensile strength (UTS), yield strength, and elongation.

3. Experimental Results

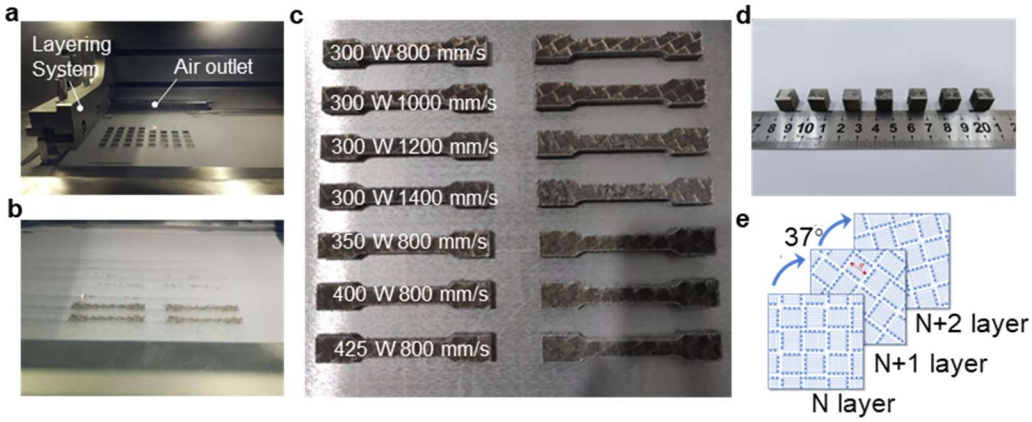

Fig. 2 Laser additive manufacturing process and sample diagram: (a) (b) LPBF forming process of 7075 aluminum alloy; (c) Tensile part; (d) Block sample; (e) 37 ° checkerboard scanning strategy for adjacent interlayer rotation

This chapter investigates the effects of varying laser power, scanning speed, and laser energy density on the densification, microstructure, and mechanical properties of 7075 aluminum alloy fabricated via Laser Powder Bed Fusion (LPBF). Optimal processing parameters were identified. The forming process and sample geometries (bulk and tensile specimens) are illustrated in Fig. 2(a)-(d). Key

ISSN: 2414-1895 DOI: 10.6919/ICJE.202506_11(6).0022

parameters include laser powers of 300 W, 350 W, 400 W, 425 W; scanning speeds of 800 mm/s, 1000 mm/s, 1200 mm/s, 1400 mm/s; and a 37° rotated chessboard scanning strategy with a chessboard size of 4.8 mm (Fig. 2(e)).

3.1 Influence of Laser Energy Density on Surface Morphology of LPBF-Processed 7075 Aluminum Alloy

Fig. 3 shows the surface morphology of LPBF-processed 7075 aluminum alloy under different laser energy densities (169 J/mm³, 208 J/mm³, 278 J/mm³, 295 J/mm³). At a low energy density (E = 169 J/mm³), the surface is rough with visible pores and spheroidization (Fig. 3 (a)). Increasing the energy density to 208 J/mm³ reduces porosity and improves densification, though surface roughness remains (Fig. 3 (b)). At 278 J/mm³, surface quality further improves with reduced roughness, but minor spatter particles persist. At 295 J/mm³, the solidification front becomes uniform, and scan tracks appear continuous and smooth, with minimal spatter and porosity (Fig. 3 (d)).

Spheroidization severely impacts the surface of specimens, and severe spheroidization will hinder the preparation of subsequent layers. The dynamic viscosity (μ) of the melt pool, expressed by Equation (2)[21-22], plays a critical role:

$$\mu=\frac{16}{15}\sqrt{\frac{m}{kT}}\sigma \tag{2}$$

where m is atomic mass, k is Boltzmann's constant, T is melt pool temperature, and σ is surface tension. The equation indicates that dynamic viscosity (μ) is inversely related to molten pool temperature (T). At low laser energy densities, the molten pool temperature is relatively low, leading to increased dynamic viscosity and reduced fluidity. Consequently, defects such as pores and irregular solidification fronts form on the specimen surface. As the laser energy density increases, the molten pool temperature rises, decreasing dynamic viscosity and enhancing fluidity. This results in a smoother surface with fewer visible defects.

Additionally, studies have shown that the significant temperature gradient in the molten pool during LPBF promotes surface tension gradients and Marangoni convection, further improving fluidity [23]. Marangoni convection refers to liquid flow driven by thermocapillary forces, which can be represented by the Marangoni number (Ma) as shown in Equation (3) [24]:

$$Ma=\frac{\Delta\sigma L}{uv_k} \tag{3}$$

where Δσ is the surface tension difference, L is the free surface length, and v_k is the kinematic viscosity. Under high laser energy densities, the reduced dynamic viscosity of the molten pool increases the Marangoni number (Ma), intensifying Marangoni convection. This drives liquid flow from regions of lower surface tension to higher surface tension and from the edges to the center of the molten pool. Therefore, under high laser energy densities, reduced viscosity enhances wettability, suppresses balling, and prolongs liquid retention time, effectively inhibiting pore formation and improving surface quality.

ISSN: 2414-1895 DOI: 10.6919/ICJE.202506_11(6).0022

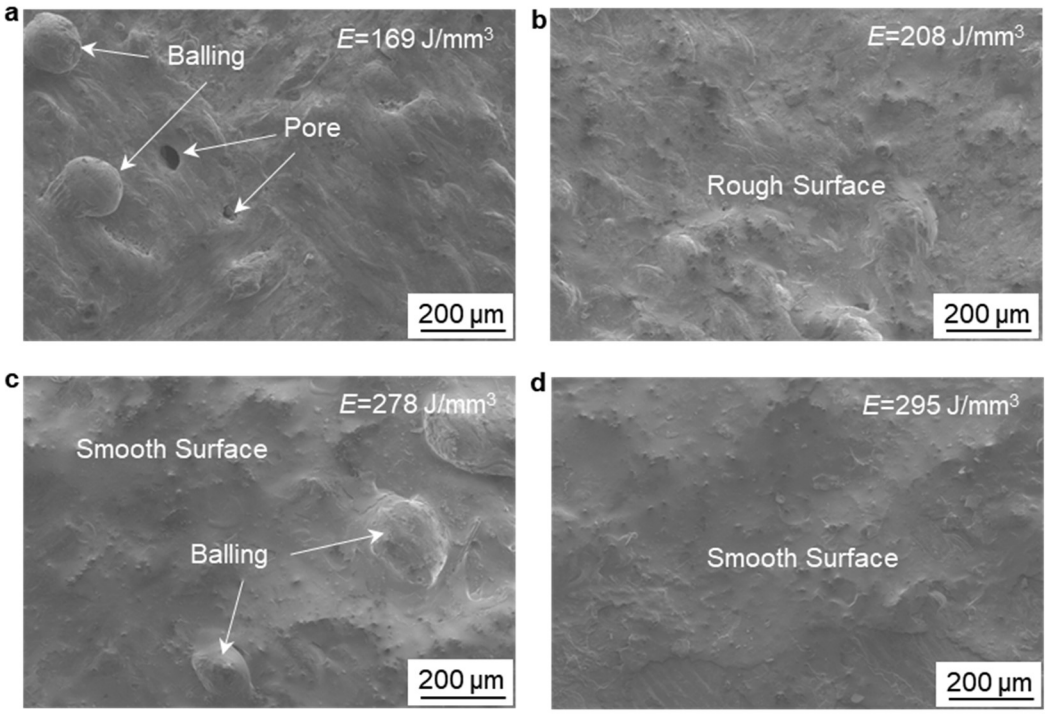

Fig. 3 SEM images of surface morphologies of LPBF-formed 7075 aluminum alloy under different laser parameters: (a) P = 300 W, v = 1000 mm/s; (b) P = 300 W, v = 800 mm/s; (c) P = 400 W, v = 800 mm/s; (d) P = 425 W, v = 800 mm/s.

3.2 Influence of Laser Energy Density on Densification and Defects in LPBF-Formed 7075 Aluminum Alloy

In the LPBF process, laser parameters significantly affect the densification level of formed specimens. Fig.4 shows optical micrographs of 7075 aluminum alloy bulk specimens parallel to the forming direction under laser powers of 300 W with scanning speeds of 800 mm/s, 1000 mm/s, 1200 mm/s, and 1400 mm/s. As the scanning speed increases and laser energy density decreases, the size of crack defects gradually reduces, while the number and size of pore defects increase. The primary cause of low material densification under these conditions is pore formation. At lower laser energy densities, the number of gas pores decreases, but irregular pores and unmelted pores increase. This is attributed to the lower molten pool temperature, where oxides adhering to the metal powder surface cannot fully melt. According to Equation(2), reduced temperature increases liquid viscosity and worsens wettability, leading to poor melt fluidity and insufficient backfilling during solidification.

Increased viscosity also weakens interlayer bonding, resulting in numerous pore defects and reduced densification. Fig.5 displays optical micrographs of 7075 aluminum alloy bulk specimens parallel to the forming direction under a scanning speed of 800 mm/s and laser powers of 300 W, 350 W, 400 W, and 425 W. Higher laser power (i.e., higher energy density) significantly reduces pore defects. For example, Fig.5 (a) shows numerous defects, including unmelted pores, gas pores, and cracks, while Fig.5 (c) exhibits fewer pores but longer cracks. At a laser energy density of 295 J/mm³ (Fig.5 (d)), forming quality improves, with reduced crack sizes and gas pores dominating porosity. However, higher energy densities cause vaporization of alloy elements in 7075 aluminum, generating metal vapor that impacts the molten pool and enlarges gas pores.

Fig.6(a) reveals that the densification of LPBF-formed 7075 aluminum alloy specimens gradually increases with laser energy density, stabilizing as energy density rises from 119 J/mm³ to 295 J/mm³, with densification improving from 96% to 98.5%. Fig.6 (b)–(c) demonstrate an inverse relationship between pore count and crack size: lower energy densities produce more pores, while higher energy densities reduce pores but increase crack dominance. Although porosity primarily governs densification, cracks under optimized parameters still severely degrade mechanical properties.

ISSN: 2414-1895 DOI: 10.6919/ICJE.202506_11(6).0022

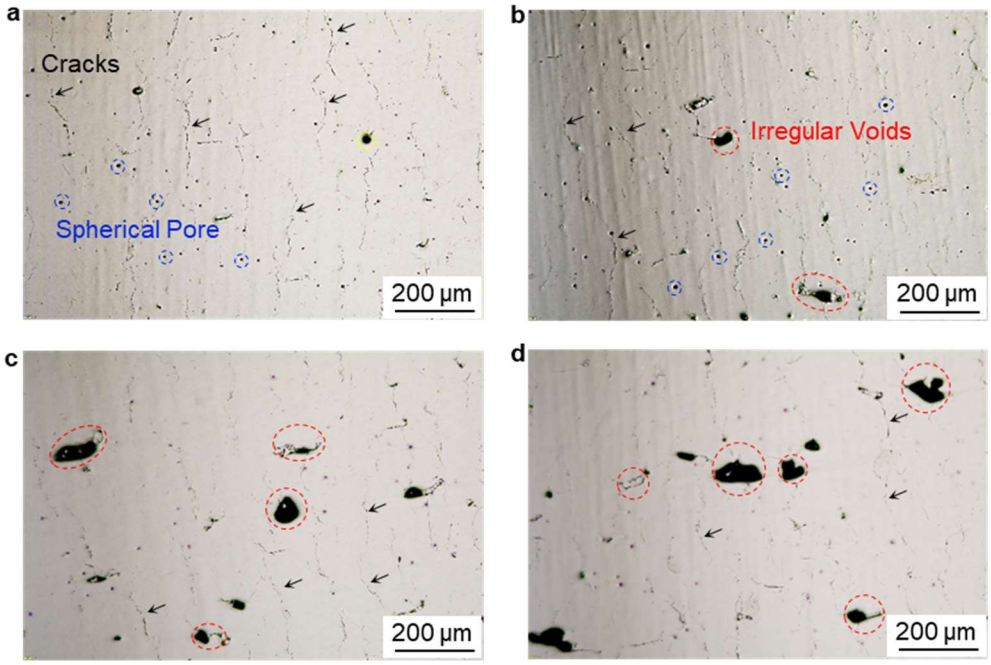

Fig. 4 Optical images of longitudinal sections of LPBF formed 7075 aluminum alloy samples at different scanning speeds at 300 W:(a) 800 mm/s, 208 J/mm3;(b)1000 mm/s, 167 J/mm3;(c)1200 mm/s, 149 J/mm3;(d)1400 mm/s, 119 J/mm^3

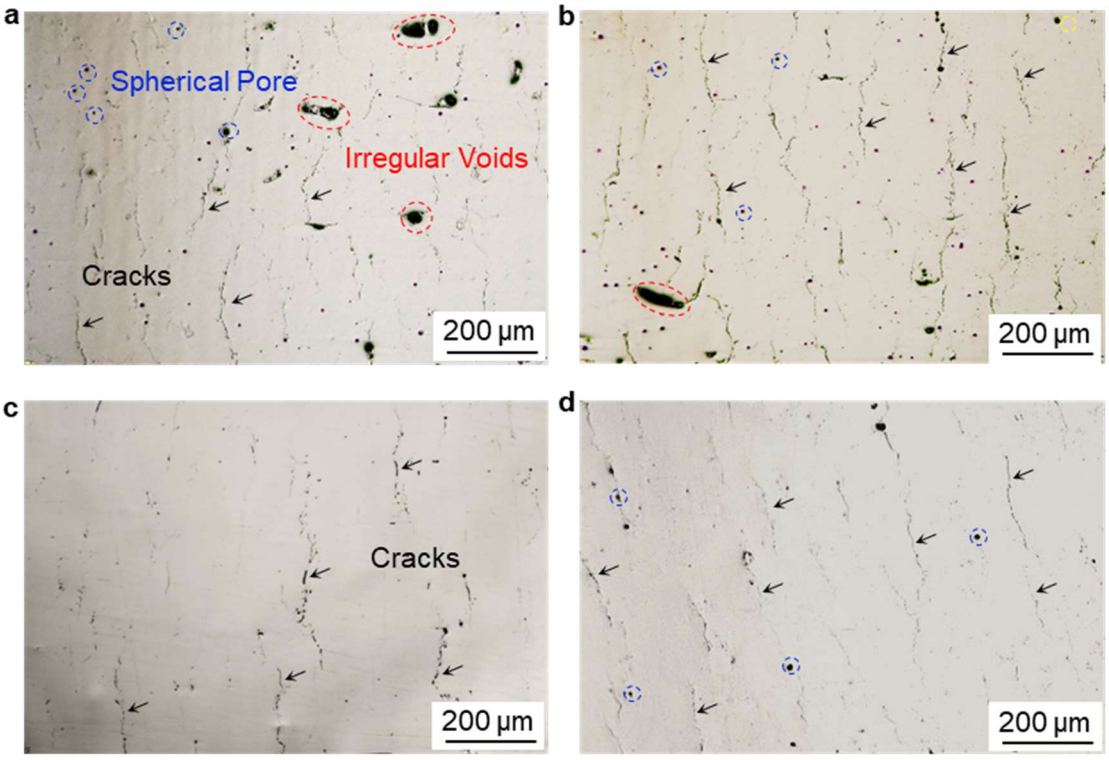

Fig. 5 Optical images of longitudinal sections of LPBF formed 7075 aluminum alloy specimens at different powers at 800mm/s: (a) 300W, 208 J/mm^3;(b)350W, 243J/mm^3;(c)400W, 278J/mm^3;(d)425 W, 295 J/mm^3

Thermal cracks in aluminum alloys arise from their inherent properties, such as wide solidification ranges, steep cooling rates, and microsegregation under non-equilibrium solidification. The high thermal conductivity of 7075 aluminum inhibits undercooling, preventing fine equiaxed grain

ISSN: 2414-1895 DOI: 10.6919/ICJE.202506_11(6).0022

formation and favoring coarse columnar grains. These grains grow epitaxially across multiple layers, forming long intergranular channels that impede liquid feeding. During solidification, residual semi-solid liquid films between grains exhibit low strength and ductility. Thermal contraction-induced tensile stresses exceeding the film's strain tolerance cause tearing. When tearing rates surpass grain growth and liquid feeding rates, cracks initiate and propagate.

At high laser energy densities, reduced melt viscosity enhances fluidity, allowing faster liquid feeding to partially heal cracks. However, increased thermal contraction stresses also promote crack formation. Fig.5 (d) shows that at 295 J/mm³, crack sizes decrease but gas pores enlarge. Thus, optimizing laser parameters can mitigate cracks but not eliminate them entirely.

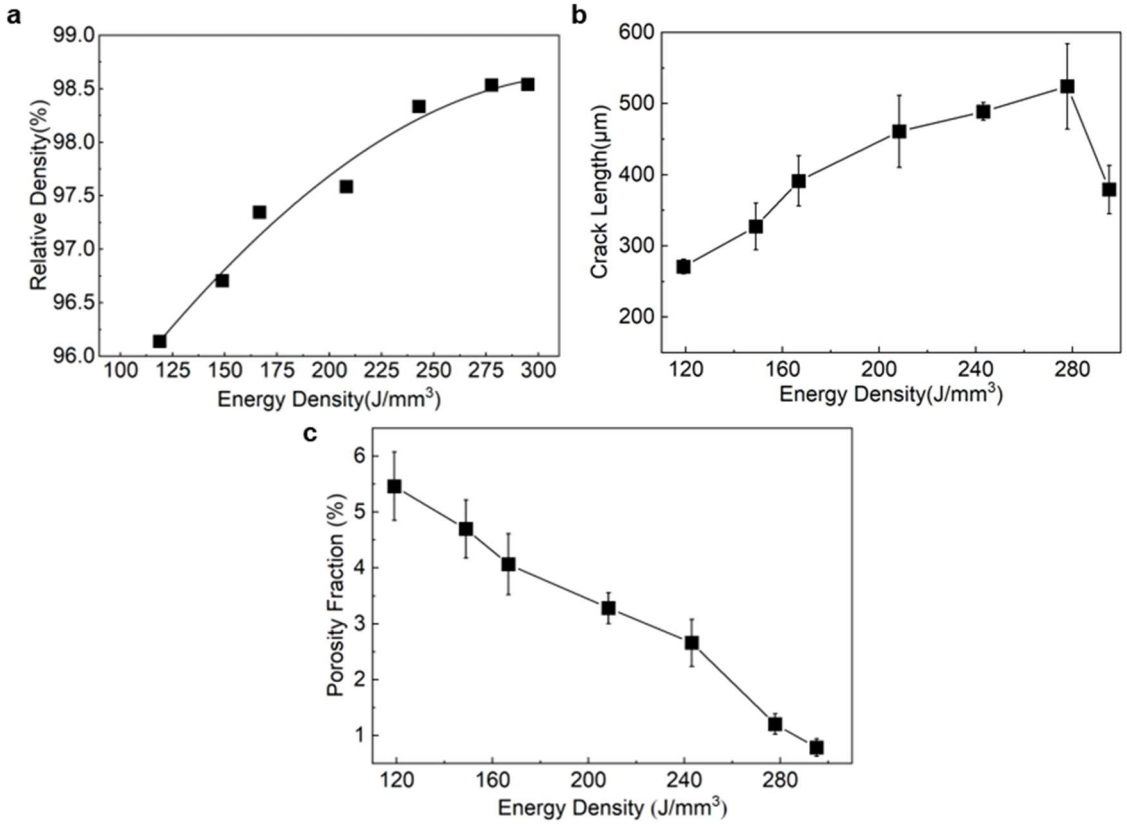

Fig. 6 The influence of laser energy density on (a) densification level, (b) average crack length, and (c) porosity of 7075 aluminum alloy formed by LPBF.

3.3 Influence of Laser Energy Density on Microstructure of LPBF-Formed 7075 Aluminum Alloy

Fig.7 shows optical micrographs of LPBF-formed 7075 aluminum alloy bulk specimens parallel to the forming direction under laser energy densities of 119 J/mm³, 167 J/mm³, 208 J/mm³, 243 J/mm³, 278 J/mm³, and 295 J/mm³. After polishing and etching, the melt pool morphology and grain structure are clearly visible. The epitaxial columnar grains observed in the metallographic images form during solidification, where crystals preferentially grow along the direction of fastest heat dissipation in regions with varying cooling conditions.

The micrographs reveal large, wavy columnar grain clusters, most of which exceed the melt pool dimensions. These columnar grains grow toward the melt pool boundaries, and their length increases with higher laser energy densities. At E = 119 J/mm³ (Fig.7(a)), columnar grains span only 2–3 melt pools. In contrast, at E = 295 J/mm³ (Fig.7(f)), they extend across tens of melt pools. Such elongated columnar grains create favorable conditions for microcrack formation. Enhanced remelting of previously solidified layers at higher energy densities promotes nucleation at the tips of columnar grains in prior melt pools. Without additional nucleation agents, grains in subsequent layers initiate

ISSN: 2414-1895 DOI: 10.6919/ICJE.202506_11(6).0022

from the endpoints of previous grains, resulting in anisotropic, epitaxially grown coarse columnar grains that span multiple melt pools. Continuous growth of these grains under laser thermal cycling is evident [24].

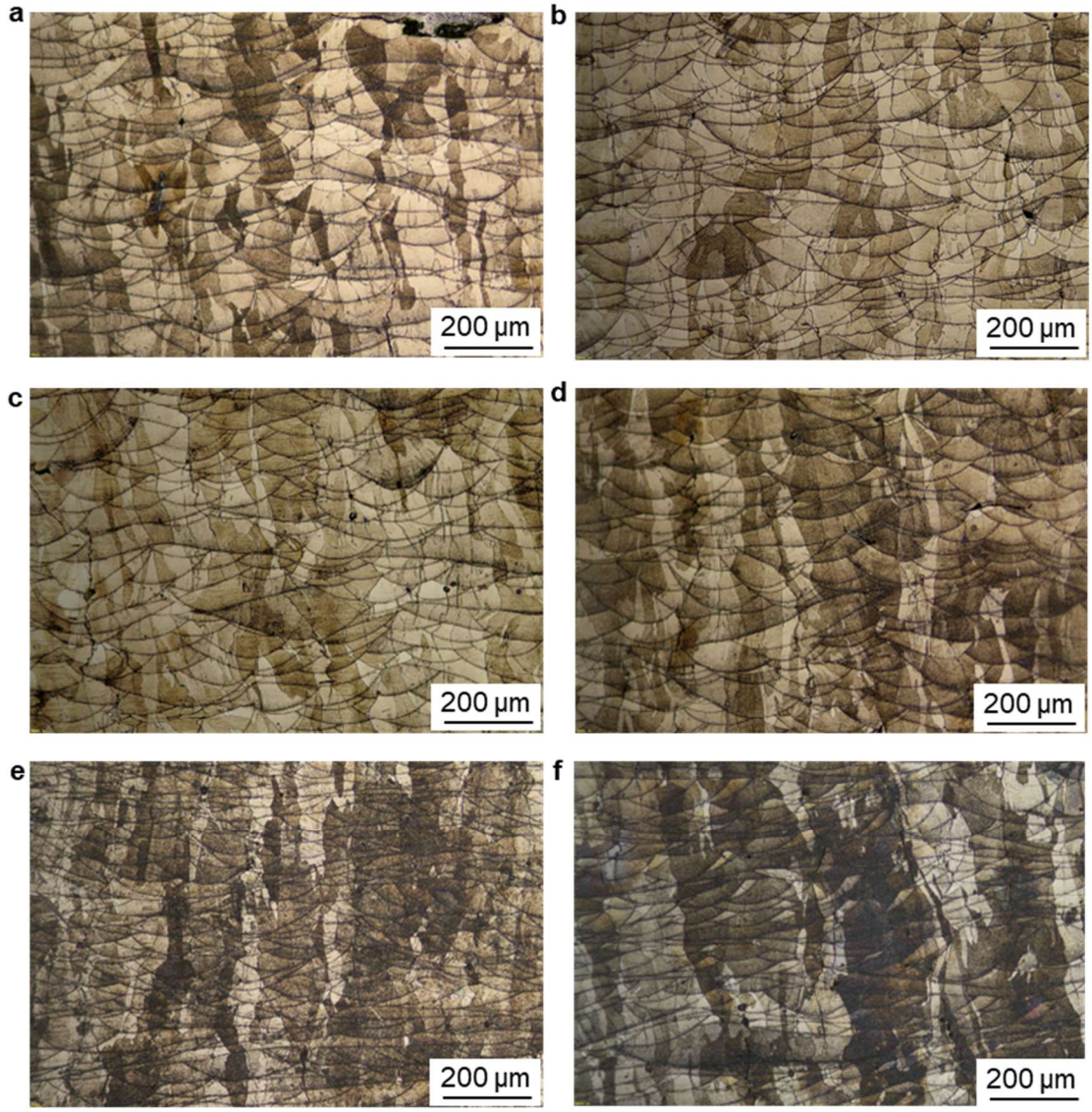

Fig. 7 Microstructure of 7075 aluminum alloy formed by LPBF under different laser energy densities: (a) E=119 J/mm^3;(b)E=167 J/mm^3;(c)E=208 J/mm^3;(d)E=243 J/mm^3;(e)E=278 J/mm^3;(f)E=295 J/mm^3

The metallographic intercept method was employed to analyze grain size distributions, as shown in Fig.8. Nine evenly distributed lines were drawn on the polished and etched micrographs (Fig.8), and the number of intersections between the lines and grain boundaries was counted. The analysis area covered 1200 × 780 μm, and the average grain diameter was calculated by dividing the actual image length by the number of intercepted grains.

Under low laser energy density (E = 119 J/mm³), statistical analysis of intercept data (Figure 8(a)) reveals the following grain size distribution: 28% of grains are smaller than 20 μm, 69% range between 20–100 μm, and 3% exceed 100 μm. As the laser energy density increases, the proportion of grains <20 μm decreases, while those ≥100 μm increases. At E = 295 J/mm³ (Figure 8(g)), the distribution shifts to 14% <20 μm, 72% between 20–100 μm, and 14% ≥100 μm.

ISSN: 2414-1895 DOI: 10.6919/ICJE.202506_11(6).0022

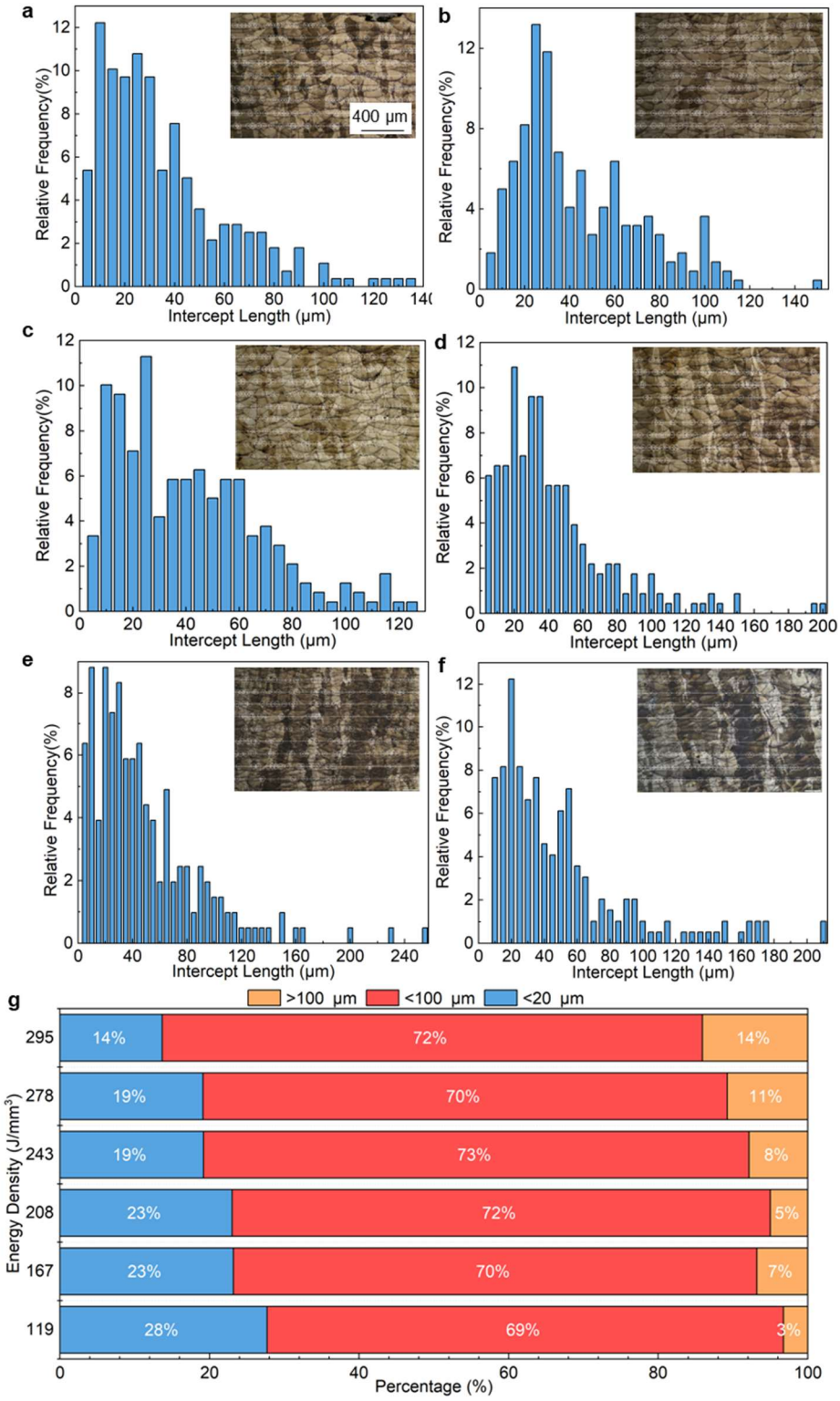

Fig. 8 Grain size distribution of LPBF formed 7075 aluminum alloy at different laser energy densities: (a) E=119 J/mm^3;(b)E=167 J/mm^3;(c)E=208 J/mm^3;(d)E=243 J/mm^3;(e)E=278 J/mm^3;(f)E=295 J/mm^3;(g) Comparison of grain size distribution.

3.4 Influence of Laser Energy Density on Mechanical Properties of LPBF-Formed 7075 Aluminum Alloy

Fig.9 presents the microhardness analysis of LPBF-formed 7075 aluminum alloy under different laser energy densities. Laser energy density significantly influences microhardness. The specimen with the highest densification level (E=295 J/mm³) achieves the maximum microhardness of 104 ± 3

ISSN: 2414-1895 DOI: 10.6919/ICJE.202506_11(6).0022

$HV_{0.1}$, exceeding other specimens under lower energy densities. As the laser energy density increases from 119 J/mm³ to 295 J/mm³, the microhardness of specimens rises significantly from 85 ± 3 $HV_{0.1}$ to 104 ± 3 $HV_{0.1}$. Additionally, fluctuations in microhardness values are observed across all specimens but slightly diminish with higher energy densities. The increase in microhardness is attributed to enhanced densification under high energy densities, while reduced fluctuations result from more complete powder melting and fewer metallurgical defects such as pores.

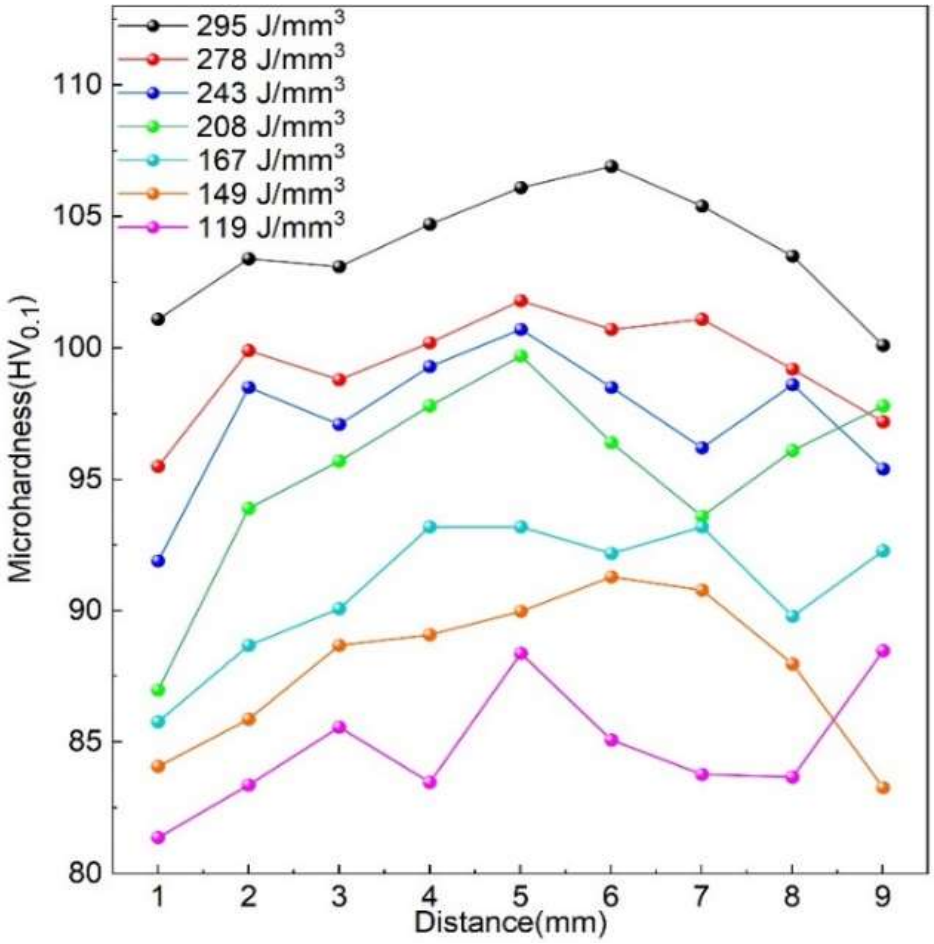

Fig. 9 Influence of laser energy density on the microhardness of LPBF-formed 7075 aluminum alloy specimens

Further tensile tests were conducted to determine the mechanical properties of LPBF-formed 7075 aluminum alloy under axial static loading. The tensile performance of the alloy was notably poor, with the highest tensile strength reaching only 60 ± 10 MPa. To clarify the fracture mechanism under static loading, fracture morphologies of specimens were analyzed (Fig.10). Cleavage steps and facets are evident at all fracture surfaces, indicating typical macroscopic brittle fracture behavior.

At E = 278 J/mm³ (Fig.10 (e)), pore defects are clearly observed at the fracture surface. A magnified view of the red-boxed region reveals a microcrack initiating from a pore. The crack morphology differs from those in Fig.5 and Fig.10 (d), exhibiting clean, straight surfaces with sharp kinks (Fig.10 (f)). Similar features are visible in Fig.10 (h). These observations confirm that pore defects during tensile loading induce crack propagation, degrading mechanical properties. Limited ductile fracture regions near solidification cracks are observed in Fig.10 (b), (d), and (h), indicating that porosity and cracks contribute to the low tensile strength of the specimens.

ISSN: 2414-1895 DOI: 10.6919/ICJE.202506_11(6).0022

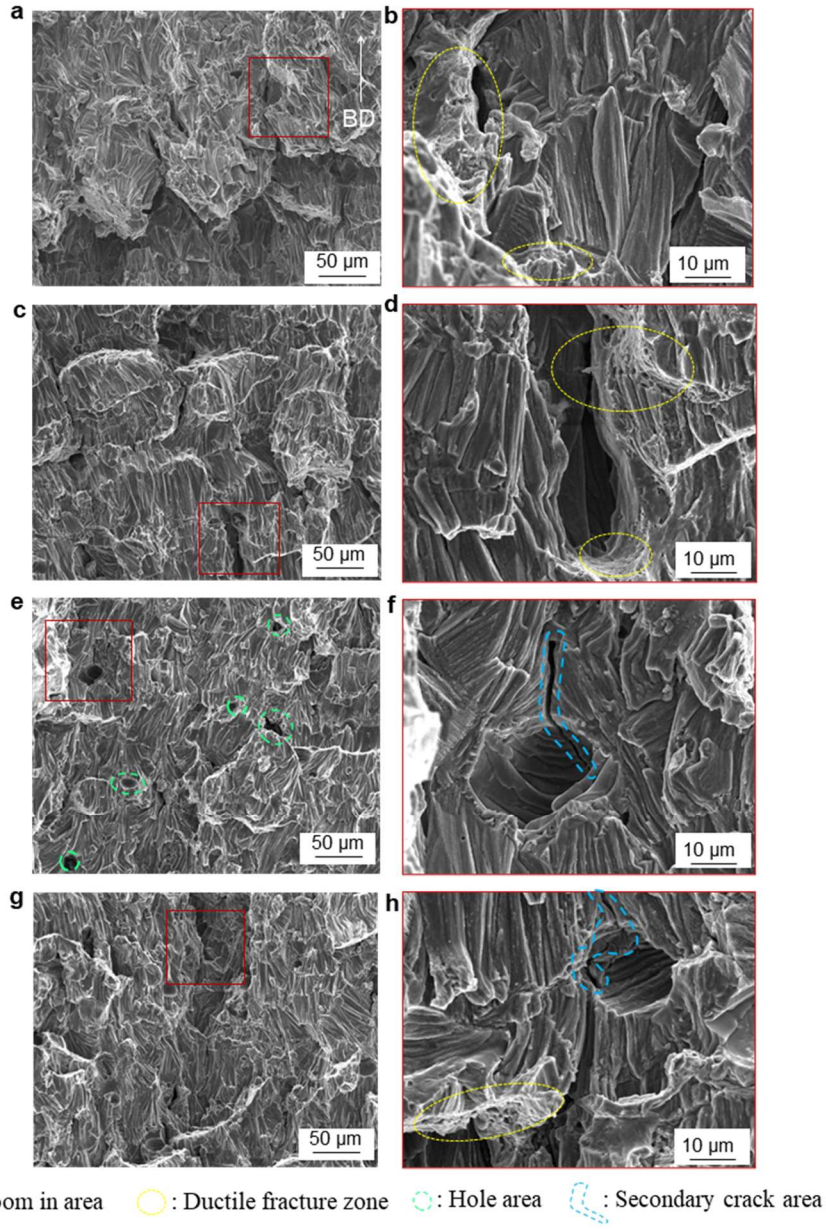

Fig.10 SEM images of tensile fracture morphologies: (a)(b) E = 208 J/mm³; (c)(d) E = 243 J/mm³; (e)(f) E = 278 J/mm³; (g)(h) E = 295 J/mm³

4. Conclusion

In this study, 7075 aluminum alloy specimens were successfully fabricated via LPBF under varying laser energy densities. The effects of scanning speed, laser power, and laser energy density on the densification, surface morphology, phase composition, microstructure, and mechanical properties of the specimens were systematically investigated. Scanning electron microscopy (SEM), backscattered electron (BSE) imaging, and the intercept method were employed to analyze the influence of laser energy density on grain size. The key conclusions are summarized as follows:

(1) Laser energy density significantly impacts the surface quality of LPBF-formed 7075 aluminum alloy.At low laser energy densities, the molten pool temperature is relatively low, leading to high liquid viscosity and weak Marangoni convection. This results in surface defects such as pores, balling phenomena, and high roughness, which adversely affect subsequent layer formation. As the laser energy density increases, the molten pool temperature rises, reducing liquid viscosity and enhancing Marangoni convection. The solidification front becomes uniform, scanning tracks grow smoother and more continuous, and surface defects are effectively suppressed.

ISSN: 2414-1895 DOI: 10.6919/ICJE.202506_11(6).0022

(2) Densification increases initially and then stabilizes with rising laser energy density.When the laser energy density increases from 119 J/mm³ to 295 J/mm³, the densification level improves from 96% to 98.5%. Crack length exhibits a positive correlation with laser energy density, while porosity shows a negative correlation, indicating that porosity is the primary factor affecting densification. Under the unique thermal conditions of LPBF, 7075 aluminum alloy grains grow epitaxially, with grain size increasing alongside energy density. At E = 119 J/mm³, grains ≥100 μm account for 3%, rising to 14% at E = 295 J/mm³.

(3) Mechanical properties of LPBF-formed 7075 aluminum alloy remain suboptimal due to porosity and cracks.The tensile strength reaches only 60 ± 10 MPa, with all specimens exhibiting brittle fracture surfaces. However, microhardness improves significantly from 85 ± 3 $HV_{0.1}$ at 119 J/mm³ to 104 ± 3 $HV_{0.1}$ at 295 J/mm³, driven by enhanced densification and reduced defects.

(4) Optimal LPBF process parameters for 7075 aluminum alloy are identified as follows:Laser energy density: 295 J/mm³,Laser power: 425 W,Scanning speed: 800 mm/s.Under these conditions, the specimen achieves the highest densification, minimal porosity, and maximum microhardness.

References

[1] Wang Guangchun. Additive Manufacturing Technology and Application Examples [M]. China Machine Press, 2014.

[2] Gu D D, Meiners W, Wissenbach K, et al. Laser additive manufacturing of metallic components: Materials, processes and mechanisms[J]. International Materials Reviews, 2012, 57(3): 133–164.

[3] Gu Dongdong, Shen Yifu. Current status and prospects of rapid prototyping of metal parts based on selective laser melting [J]. Aeronautical Manufacturing Technology, 2012, 8: 6.

[4] Abd-Elaziem W, Elkatatny S, Abd-Elaziem A, et al. On the current research progress of metallic materials fabricated by laser powder bed fusion process: a review[J]. Journal of Materials Research and Technology, 2022, 20: 681–707.

[5] Li Y, Gu D. Parametric analysis of thermal behavior during selective laser melting additive manufacturing of aluminum alloy powder[J]. Materials and Design, 2014, 63: 856–867.

[6] Azizi A, Chen X B, Gou F L, et al. Selective laser melting of metal structures onto graphite substrates via a low melting point interlayer alloy[J]. Apply Materials Taday, 2022, 26: 101334.

[7] Chen Keyu, Xu Limin, Gan Jie. Influence of laser power on microstructure and mechanical properties of AlSi10Mg fabricated by selective laser melting [J]. Laser & Optoelectronics Progress, 2021, 58(13): 347–355.

[8] Miranda G, Faria S, Bartolomeu F, et al. A study on the production of thin-walled Ti6Al4V parts by selective laser melting[J]. Journal of Manufacturing Processes, 2019, 39: 346–355.

[9] Al-Rubaie K S, Melotti S, Rabelo A, et al. Machinability of SLM-produced Ti6Al4V titanium alloy parts[J]. Journal of Manufacturing Processes, 2020, 57: 768–786.

[10] Zhang H, Gu D, Ma C, et al. Effect of post heat treatment on microstructure and mechanical properties of Ni-based composites by selective laser melting[J]. Materials Science and Engineering A, 2019, 765: 138294.

[11] Gu D, Zhang H, Dai D, et al. Laser additive manufacturing of nano-TiC reinforced Ni-based nanocomposites with tailored microstructure and performance[J]. Composites Part B: Engineering, 2019, 163: 585–597.

[12] Grzesiak D, AlMangour B, Krawczyk M, et al. Selective laser melting of TiC reinforced stainless steel nanocomposites: Mechanical behaviour at elevated temperatures[J]. Materials Letters, 2019, 256: 126633.

[13] Yan Q, Song B, Shi Y. Comparative study of performance comparison of AlSi10Mg alloy prepared by selective laser melting and casting[J]. Journal of Materials Science and Technology, 2020, 41: 199–208.

[14] Liu X, Zhao C, Zhou X, et al. CNT-reinforced AlSi10Mg composite by selective laser melting: microstructural and mechanical properties[J]. Materials Science and Technology (United Kingdom), 2019, 35(9): 1038–1045.

ISSN: 2414-1895 DOI: 10.6919/ICJE.202506_11(6).0022

[15] Williams J C, Starke E A. Progress in structural materials for aerospace systems[J]. Acta Materialia, 2003, 51(19): 5775–5799.

[16] Kaufmann N, Imran M, Wischeropp T M, et al. Influence of process parameters on the quality of aluminium alloy en AW 7075 using Selective Laser Melting (SLM)[J]. Physics Procedia, 2016, 83: 918–926.

[17] Babu A P, Kairy S K, Huang A, et al. Laser powder bed fusion of high solute Al-Zn-Mg alloys: Processing, characterisation and properties[J]. Materials and Design, 2020, 196.

[18] Louvis E, Fox P, Sutcliffe C J. Selective laser melting of aluminium components[J]. Journal of Materials Processing Technology, 2011, 211(2): 275–284.

[19] Stopyra W, Gruber K, Smolina I, et al. Laser powder bed fusion of AA7075 alloy: Influence of process parameters on porosity and hot cracking[J]. Additive Manufacturing, 2020, 35: 101270.

[20] Wang Dayuan, Li Xiaoqiang, Lai Jiaming, et al. Study on microstructure, properties, and cracks of 7075 aluminum alloy fabricated by selective laser melting [J]. Applied Laser, 2019, 39.

[21] Gu D, Shen Y. Effects of processing parameters on consolidation and microstructure of W-Cu components by DMLS[J]. Journal of Alloys and Compounds, 2009, 473(1–2): 107–115.

[22] Arafune K, Hirata A. Thermal and solutal marangoni convection in In-Ga-Sb system[J]. Journal of Crystal Growth, 1999, 197(4): 811–817.

[23] Yogamalar R, Srinivasan R, Vinu A, et al. X-ray peak broadening analysis in ZnO nanoparticles[J]. Solid State Communications, 2009, 149(43–44): 1919–1923.

[24] Prasad A, Yuan L, Lee P, et al. Towards understanding grain nucleation Manufacturing solidification conditions under Additive[J]. Acta Materialia, 2020, 195: 392–403.